



Anomalous elastic buckling of layered crystalline materials in the absence of structure slenderness



Manrui Ren^a, Yilun Liu^b, Jefferson Zhe Liu^{c,*}, Lifeng Wang^d, Quanshui Zheng^{a,*}

^a Department of Engineering Mechanics, Center for Nano and Micro Mechanics, and Applied Mechanics Lab, Tsinghua University, Beijing 100084, China

^b State Key Laboratory for Strength and Vibration of Mechanical Structures, School of Aerospace Engineering, Xi'an Jiaotong University, Xi'an 710049, China

^c Department of Mechanical and Aerospace Engineering, Monash University, Clayton, VIC 3800, Australia

^d Department of Mechanical Engineering, Stony Brook University, Stony Brook, NY 11794-2300, United States

ARTICLE INFO

Article history:

Received 27 May 2014

Received in revised form

11 December 2015

Accepted 14 December 2015

Available online 17 December 2015

Keywords:

Layered crystalline materials

Intrinsic buckling strain

Size effect

Shear buckling mode

Extreme elasticity anisotropy

ABSTRACT

Layered crystalline materials, such as graphene, boron nitride, tungsten sulfate, phosphorene, etc., have attracted enormous attentions, due to their unique crystal structures and superior mechanical, thermal, and physical properties. Making use of mechanical buckling is a promising route to control their structural morphology and thus tune their physical properties, giving rise to many novel applications. In this paper, we employ molecular dynamics (MD) simulations and theoretical modeling to study the compressive buckling of a column made of layered crystalline materials with the crystal layers parallel to the compressive direction. We find that the mechanical buckling of the layered crystalline materials exhibits two anomalous and counter-intuitive features as approaching the zero slenderness ratio. First, the critical buckling strain ϵ_{cr} has a finite value that is much lower than the material's elastic limit strain. A continuum mechanics model (by homogenizing the layered materials) is proposed for the ϵ_{cr} , which agrees well with the results of MD simulations. We find that the ϵ_{cr} solely depends on elastic constants without any structural dimension, which appears to be an intrinsic material property and thus is defined as intrinsic buckling strain (IBS), ϵ_{cr}^{IBS} , in this paper. Second, below a certain nanoscale length, l_0 , in the compressive direction (e.g., about 20 nm for graphite), the critical buckling strain ϵ_{cr} shows a size effect, i.e., increasing as the column length L decreases. To account for the size effect, inspired by our recently developed multi-beam shear model (Liu et al., 2011), a bending energy term of individual crystal layer is introduced in our continuum model. The theoretical model of ϵ_{cr} agrees well with the size effects observed in MD simulations. This study could lay a ground for engineering layered crystalline materials in various nano-materials and nano-devices via mechanical buckling.

© 2015 Elsevier Ltd. All rights reserved.

1. Introduction

Buckling, as a mechanical instability, is a common phenomenon in nature (Gere and Timoshenko, 1998; Price and Cosgrove, 1990; Zartman and Shvartsman, 2010). It is often treated as a nuisance to be avoided. This view is changing with

* Corresponding authors.

E-mail addresses: zhe.liu@monash.edu (J. Zhe Liu), zhengqs@tsinghua.edu.cn (Q. Zheng).

the growing knowledge of this phenomenon (Biot, 1957; Bowden et al., 1998; Brau et al., 2010; Budd et al., 2003; Efimenko et al., 2005; Gere and Timoshenko, 1998; Hohlfield and Mahadevan, 2011; Huang et al., 2005; Hunt et al., 2000; Kim et al., 2011; Pociavsek et al., 2008; Wadde et al., 2004) and the emerging successful cases of employing mechanical buckling in real applications (Efimenko et al., 2005; Guo et al., 2011; Kim et al., 2008; Kim et al., 2009; Kim et al., 2010; Koo et al., 2010; Rogers et al., 2010; Stafford et al., 2004; Wang et al., 2011; Zang et al., 2013). For example, utilizing buckled interconnecting components in electronic devices leads to “stretchable electronics” that can accommodate large stretching and compressive loads without breaking (Kim et al., 2008; Rogers et al., 2010). Mechanical buckling of a thin stiff film on a soft substrate under an in-plane compression can alter the surface morphology and thus modulate the surface physicochemical properties, giving rise to various applications, such as artificial skins (Efimenko et al., 2005), micro-devices to measure mechanical properties of thin polymer and nanoparticle films (Leahy et al., 2010; Stafford et al., 2004), dynamically controlled surface wettability (Zang et al., 2013), enhancement of light extracting efficiency from organic light-emitting diodes (Koo et al., 2010), and dynamic display of biomolecule micropatterns (Kim et al., 2009). The surface ripples also have many applications in micro-fluidic devices (Efimenko et al., 2005) and artificial muscle actuators (Zang et al., 2013).

The discovery of graphene (Novoselov et al., 2004) has stimulated intensive research interests for two dimensional crystalline materials, such as BN, MoS₂, WS₂, silicene, graphyne, and so on (Golberg et al., 2010; Malko et al., 2012; Nicolosi et al., 2013; Vogt et al., 2012; Wang et al., 2012; Wilson and Yoffe, 1969). For this class of materials, atoms distributed in a layered crystal lattice are bonded via strong chemical bonds, whereas different crystal layers interact with each other through weak van der Waals or electrostatic forces. Such a two dimensional crystalline material has a unique combination of structural, mechanical and physical properties, enabling great potentials for applications in electronic devices, catalysts, batteries, and super-capacitors, as seen in recent extensive experimental and theoretical studies (Geim and Novoselov, 2007). In practice, these materials are often fabricated in a form with multiple crystal layers stacked together, either for the convenience of fabrication or intentionally. For example, tuning either the number of layers or the stacking sequence of different types of crystal layers can modulate electronic properties of the resultant van der Waals heterostructures (Geim and Grigorieva, 2013; Haigh et al., 2012). It turns out that using multi-layers of graphene as a building block of graphene cellular foams is essential for the observed super-elasticity under a large compressive strain up to 80% in experiments (Qiu et al., 2012).

In addition to the widely studied approaches to tailor the physical properties of layered crystalline materials, e.g., scissoring graphene into different shapes (Ci et al., 2008), chemical doping (Ci et al., 2010), chemical or physical adsorption (Elias et al., 2009; Nair et al., 2010; Schedin et al., 2007; Xu et al., 2009), mechanical buckling caused by a compressive load parallel to the basal planes can serve as a promising method to enable new applications. There are already several successful experimental studies. It has been reported that the reversible mechanical buckling of a stack of graphene-oxide layers is the origin for the hydration responsive property of graphene oxide liquid crystal in experiments (Guo et al., 2011). The periodically rippled graphene ribbons formed on a pre-stretched elastomer substrate can be used as high performance strain sensors (Wang et al., 2011). A super-hydrophobic surface with a reversibly tunable wettability has been realized using crumpled graphene films (Zang et al., 2013). However, employing mechanical buckling of layered crystalline materials in applications is still hampered by inadequate understanding of this phenomenon.

The most well-known elastic buckling is the bending mode of instability studied back to Euler's era (Gere and Timoshenko, 1998). For a slender structure, such as a beam, plate, or thin film, being subject to a longitudinal compression, lateral deflection will occur beyond a critical load. This is because bending is energetically less costly than compression for these slender structures. Most of the applications described previously are based on this type of instability. It should be noted that the unique atomistic structures of layered materials, i.e., strong in-plane covalent chemical bonds, giving rise to a very high in-plane elastic modulus, and weak out-of-plane van der Waals or electrostatic interactions, yielding a very small interlayer shear modulus, imply that the interlayer shear effect plays an important role in the mechanical behaviors of layered materials (Ghosh and Arroyo, 2013; Li et al., 2007; Liu et al., 2001; Liu et al., 2011; Yu, 2004). For the layered materials, above a critical compressive load along in-plane directions, shear mode instability occurs. The shear deformation among adjacent atomic layers generates a lateral displacement and then releases the compressive strain. Such a shear mode of instability was observed in wood (Byskov et al., 2002), fiber reinforce composites (Budiansky et al., 1998; Kyriakides et al., 1995), and geological strata (Price and Cosgrove, 1990). However, there are very few experimental and theoretical studies for the shear mode instability of the layered crystalline solids (Cranford, 2013; Liu et al., 2010; Ren et al., 2015), particularly in terms of the critical buckling load. It should be noted that the internal buckling of anisotropic medium was theoretically studied previously, as reviewed in Biot's book (Biot, 1965) and a recent book from Bažant (Bažant and Cedolin, 2010). But there are two limitations. First, these previous theoretical studies are continuum mechanics models and the validation of continuum modeling to the layered crystalline materials at nanoscale is ambiguous. Second, the previous theoretical studies of internal buckling usually assumed the anisotropic materials incompressible (Bažant and Cedolin, 2010; Biot, 1965), which is inconsistent to most layered crystalline materials.

In this paper, we firstly employ molecular dynamics (MD) simulations to simulate the mechanical buckling of graphite, hexagonal boron nitride (*h*-BN), virtual graphite, and virtual *h*-BN (i.e., parameters of Lennard-Jones potential used to describe the interlayer van der Waals interaction are altered to tune the interlayer shear modulus) at a nanometer scale in Section 2. In Section 3, a continuum mechanics model is developed to describe the buckling behaviors of a column with an infinite width (i.e., zero slenderness ratio) made of layered crystalline materials. In this model, the layered materials are assumed as homogenous medium of transversely isotropic elasticity. This continuum mechanics model provides accurate

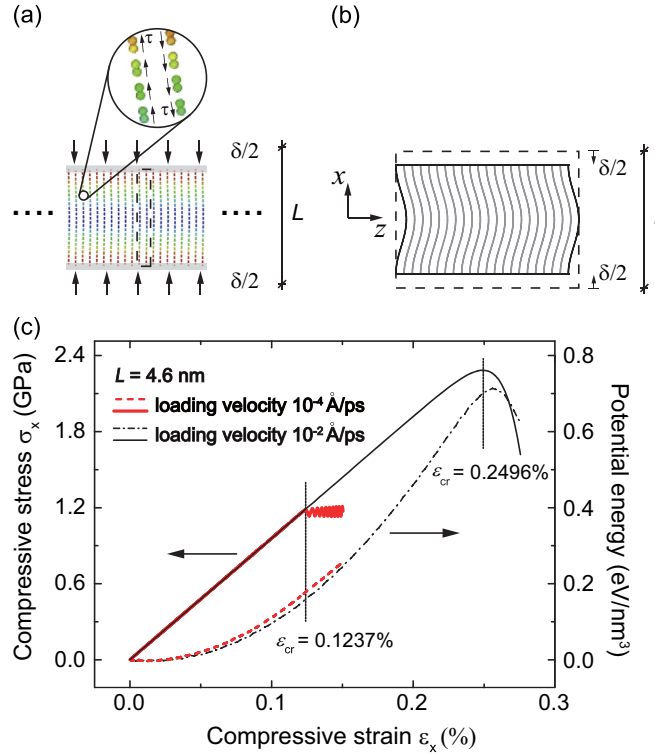


Fig. 1. (a) Molecular model for mechanical buckling of a graphite column in NEMD simulations. Graphene basal planes are parallel to the x - y plane. The box enclosed by dashed lines represents the super-cell. Periodic boundary conditions are applied in all three directions. Note that the periodic boundary conditions applied in lateral directions imply an infinite gyration radius ρ and thus lead to a zero slenderness ratio L/ρ . The super-cell is compressed in x direction at a constant velocity which varies from 10^{-5} up to 1 \AA/ps in different simulations, meanwhile the y and z dimensions of the super-cell are fixed and the three super-cell vectors remain perpendicular to each other through the simulations. The color map illustrates relative magnitude of the lateral displacement (z) after mechanical buckling, in which the blue color denotes a larger displacement than the red color. (b) A sketch of the buckling shape. (c) Potential energy and stress σ_x versus compressive strain ϵ_x in MD simulations. At the critical point, the potential energy and stress results show an abrupt change, indicating the happening of mechanical buckling. (For interpretation of the references to color in this figure legend, the reader is referred to the web version of this article.)

predictions for the critical buckling strain ϵ_{cr} down to a column length L of about 20 nm in MD simulations. A theoretical model for a more general case (orthorhombic crystalline symmetry) is presented in appendix. Section 4 presents a continuum model to explain the observed size effect of the ϵ_{cr} in MD simulations. A length parameter l_0 is defined. In case of the column length L being larger than l_0 , the size effect is becoming negligible. Section 5 discusses the implications of such elastic buckling in layered crystalline materials and its potential applications. Conclusions are drawn in Section 6.

2. MD simulations

In light of great potentials of utilizing mechanical buckling in nano devices (Koo et al., 2010; Rogers et al., 2010; Zang et al., 2013), it is of great interests to investigate this phenomenon at a nanometer scale for the layered crystalline materials. In this section, non-equilibrium molecular dynamics (NEMD) simulations is employed to study the elastic buckling of the hexagonal layered crystalline materials, e.g. graphite, h -BN, virtual-graphite, and virtual h -BN columns with a length L down to 2 nm.

Fig. 1(a) depicts our molecular system: a graphite column composed of periodic A/B stacked graphene layers (normal to the z -axis) with their basal planes parallel to the longitudinal axis (the x -axis) and the transverse axis (the y -axis). Longitudinal length L is selected between 2 nm and 40 nm. Periodic boundary conditions (PBC) are applied in all three coordinate directions. The dashed box in Fig. 1(a) represents the super-cell used in our MD simulations. The super-cell is compressed in the x direction at a constant velocity which varies from 10^{-5} to 1 \AA/ps in different simulations, meanwhile the y and z dimensions of the super-cell are fixed and the three super-cell vectors remain perpendicular to each other through the simulations. The PBC along the x -axis restricts wavelength of the first-order buckling as L . The PBC in the y and z directions result in an infinite radius of gyration ρ of the cross-section (i.e., $\rho \sim \infty$). Thus our molecular models have a ratio of slenderness $L/\rho = 0$.

NEMD simulations are performed using the LAMMPS code (Plimpton, 1995). The adaptive intermolecular reactive empirical bond order (AIREBO) potential (Stuart et al., 2000) is adopted to describe the interatomic interactions of the graphite

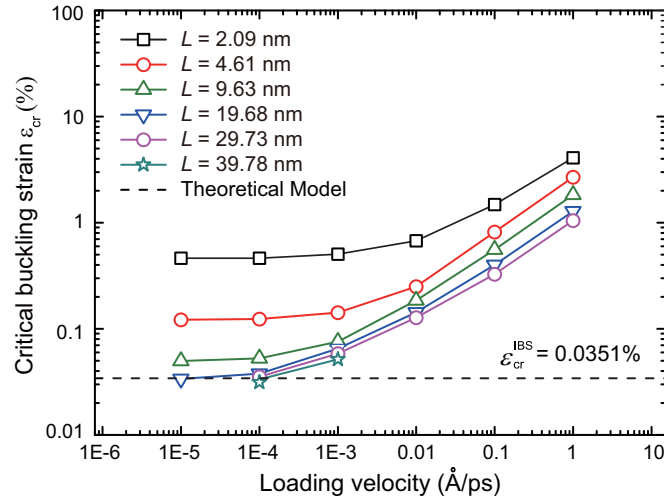


Fig. 2. Critical elastic buckling strain ε_{cr} of a graphite column (Fig. 1(a)) as a function of loading velocity in NEMD simulations. Results for different longitudinal length L from 2.09 nm to 39.78 nm are shown. Note that the PBC in y and z directions result in an infinite radius of gyration ρ of the cross-section (i.e., $\rho \sim \infty$). Thus all MD models have a ratio of slenderness $L/\rho = 0$. Prediction from the continuum mechanics model Eq. (12) in Section 3 is shown as the dashed line for a comparison.

column. Temperature of the whole system is fixed at 0.1 K using the Berendsen thermostat, with the temperature calculated after removing the center-of-mass velocity. A time step of 1.0 fs is used and the simulations are continued until the elastic buckling took place. Although the interlayer delamination has been observed in the post-buckling of multilayer graphene (Cranford, 2013), in this work we just care about the critical buckling strain and the interlayer delamination does not occur for all of the cases in our MD simulations.

For a column with $L = 4.6$ nm, Fig. 1(c) shows the results of potential energy and stress σ_x as functions of compressive strain ε_x in the x direction, at two different loading velocities 10^{-4} Å/ps and 10^{-2} Å/ps. The strain is defined as $\varepsilon_x = \delta/L$, where δ is the change of the unit cell in x -dimension. The results of potential energy and the stress in the x -direction can be directly output from LAMMPS. In the beginning, both potential energy results appear as a parabolic function of the strain ε_x . This is consistent to the obtained linear stress–strain relations in Fig. 1(c). At the critical point, the energy curves start to deviate from the parabolic relation and accordingly the stress curves exhibit a significantly drop, indicating the happening of mechanical buckling. Indeed, the carbon atoms exhibit a clear lateral displacement in the z direction after the critical point. Color-map in Fig. 1(a) shows the relative magnitude of lateral displacement obtained at a loading velocity of 10^{-4} Å/ps, in which the blue color denotes a relatively larger displacement than the red color. Fig. 1(b) sketches the buckling shape. Fig. 1(c) shows that the determined critical compressive strain value ε_{cr} sensitively depends on the loading velocity. At 10^{-2} Å/ps, the ε_{cr} equals to 0.250%, whereas at a lower loading velocity of 10^{-4} Å/ps the critical strain result significantly reduces to $\varepsilon_{cr} = 0.124\%$. This is a common phenomenon in dynamic buckling (Lindberg, 2003). After release of the compressive load, the buckled graphite column bounces back, fully recovering its original shape.

Fig. 2 summarizes the dependence of ε_{cr} on the loading velocity for a graphite column with different length L from about 2–40 nm. Reduction of the loading velocity generally leads to a decrease of obtained ε_{cr} values. Apparently, a convergence is achieved below 10^{-4} Å/ps. A close inspection of the data in Table 1 indicates the difference of ε_{cr} is indeed very small for loading velocity of 10^{-4} Å/ps and 10^{-5} Å/ps. In addition, it is found that a shorter column has a higher convergent ε_{cr} result. Above $L \sim 20$ nm, only a minor difference is observed in the ε_{cr} value at loading velocity of 10^{-4} Å/ps, i.e., between 0.038% and 0.034%. In the following, we will denote the critical strain determined for a graphite column with length $L \geq 20$ nm and at a loading velocity $\leq 10^{-4}$ Å/ps in MD simulations as the converged ε_{cr} .

The NEMD simulations were also carried out for a column made of *h*-BN, some *virtual* graphite, and *virtual h*-BN (similar to Fig. 1(a)) to determine their critical buckling strain. The virtual material models were created by artificially changing the parameter ε or σ in the LJ potential that were used to describe the interlayer van der Waals interaction. Table 2 lists the parameters of the original LJ potentials. Given that the predicted C_{44} value from the AIREBO force field for graphite is far smaller than the experimental results (discussed later), the value of ε is increased by 2–10 times (Table 3). The in-plane interaction of a graphene

Table 1

The critical buckling strain ε_{cr} of a graphite column with different length L under a (low) loading velocity of 10^{-4} or 10^{-5} Å/ps.

L (nm)	2.09	4.61	9.63	19.68	29.73	39.78
10^{-4} Å/ps	0.464%	0.124%	0.0525%	0.0378%	0.0353%	0.0334%
10^{-5} Å/ps	0.464%	0.122%	0.0498%	0.0337%	–	–

Table 2

Parameters of the Lennard-Jones potential used to describe the interlayer van der Waals interactions for graphite and *h*-BN in our NEMD simulations.

Atom pair	ϵ (meV)	σ (Å)	References
C-C	2.84	3.40	(Stuart et al., 2000)
B-B	4.116	3.45	(Baowan and Hill, 2007)
N-N	6.281	3.365	(Baowan and Hill, 2007)
B-N	5.085	3.41	(Baowan and Hill, 2007)

Table 3

A comparison of the converged ϵ_{cr} results from NEMD simulations ($L = 19.69$ nm and low loading velocity of 10^{-5} Å/ps) and our theoretical model ϵ_{cr}^{IBS} [Eq. (12)]. The calculated elastic modulus C_{11} and C_{44} are shown as well.

L-J parameter	C_{11} (GPa)	C_{44} (GPa)	Continuum mechanics model	MD simulation
Graphite ^a	980	0.3442	0.03512%	0.03370%
Graphite (ϵ, σ) ^b	1221	0.3329	0.02727%	0.03482%
Virtual Graphite ($2\epsilon, \sigma$) ^b	1248	0.6671	0.05343%	0.06115%
Virtual Graphite ($5\epsilon, \sigma$) ^b	1273	1.677	0.1317%	0.1425%
Virtual Graphite ($7\epsilon, \sigma$) ^b	1288	2.3563	0.1829%	0.1899%
Virtual Graphite ($10\epsilon, \sigma$) ^b	1309	3.3844	0.2586%	0.2656%
Virtual Graphite ($10\epsilon, 1.1\sigma$) ^b	1204	2.5678	0.2133%	0.2359%
Virtual Graphite ($10\epsilon, 1.2\sigma$) ^b	1110	2.0176	0.1817%	0.2048%
Virtual Graphite ($10\epsilon, 1.3\sigma$) ^b	1035	1.7493	0.1691%	0.1912%
Virtual Graphite ($10\epsilon, 1.4\sigma$) ^b	971	1.5497	0.1596%	0.1863%
<i>h</i> -BN ^c	832	0.6254	0.07518%	0.1082%
Virtual <i>h</i> -BN ($10\epsilon, \sigma$) ^c	884	6.3725	0.7211%	0.7441%

^a modeled by AIREBO force field.

^b modeled by Tersoff and LJ potentials. The value of parameter ϵ in LJ potential is increased by 2, 5, 7, and 10 times, respectively and the value of parameter σ in LJ potential is increased by 1.1, 1.2, 1.3, and 1.4 times, respectively. Before the NEMD simulations and the calculations for C_{44} , interlayer distances and C–C bond lengths are optimized to remove residual stresses.

^c modeled by Tersoff and LJ potentials. The value of parameter ϵ in LJ potential is increased by 1 and 10 times, respectively. Before the NEMD simulations and the calculations for C_{44} , interlayer distances and B–N bond lengths are optimized to remove residual stresses.

layer or *h*-BN layer is described using the Tersoff potentials (Kinaci et al., 2012; Tersoff, 1989). To avoid the dynamic effect, we adopted a low loading velocity of 10^{-5} Å/ps. Note that for the graphite columns, the results of ϵ_{cr} determined using Tersoff and LJ potentials are similar to those using AIREBO potential (Table 3). A similar dependence of ϵ_{cr} on the column length L is observed in Fig. 3. As L increases above ~ 20 nm, the critical buckling strain approaches a converged value ϵ_{cr} .

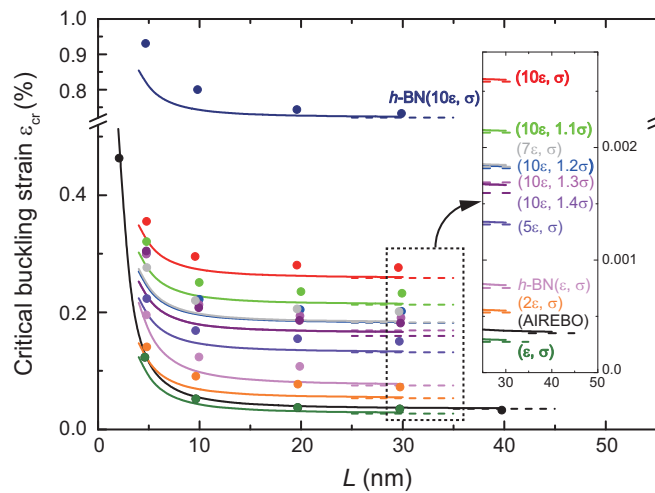


Fig. 3. The critical buckling strain results of a column made of different layered materials as a function of column length L determined in MD simulations using Tersoff and LJ potentials. Different materials are represented by their corresponding LJ parameters (ϵ, σ) and the notations without “*h*-BN” represent (virtual) graphite by default (cf. Table 3). Results using AIREBO potential for graphite are also included for comparison. To avoid the dynamic effect, a low loading velocity of 10^{-5} Å/ps is adopted. Note that the PBC in y and z directions results in an infinite radius of gyration ρ of the cross-section and thus a zero slenderness ratio for all MD models. The predictions of the continuum theoretical model Eq. (12) in Section 3 are shown as dashed lines. The solid lines represent the theoretical model Eq. (18) in Section 4, which is developed to account for the observed size effect in MD.

Table 3 summarises the converged ϵ_{cr} values for all different material models at $L=19.68$ nm and a loading velocity of 10^{-5} Å/ps. Interestingly, the buckling strain values are lower than 1%, which is far lower than the mechanical strength of graphene and *h*-BN (Lee et al., 2008; Song et al., 2010). This suggests such a mechanical buckling is, in principle, achievable in experiments. More interestingly, this mechanical buckling phenomenon takes place at a zero slenderness ratio, which is believed to be highly unlikely for conventional isotropic materials. For the virtual materials, increasing the parameter ϵ of the LJ potential (*i.e.*, enhancing interlayer binding strength) leads to a higher converged ϵ_{cr} value, whereas increasing the parameter σ in the LJ potential (*i.e.*, enlarging the equilibrium interlayer distance) results in a lower converged ϵ_{cr} value. This observation will be explained in Section 3.

According to the continuum mechanics models derived in Sections 3 and 4, the interlayer shear modulus and the elastic modulus in the compressive direction, namely C_{44} and C_{11} , are the determinant parameters for the converged ϵ_{cr} value. These two moduli should be calculated using the same force fields adopted in MD simulations. The C_{11} modulus is determined by fitting the potential energy curve as a function of strain $U=1/2C_{11}\epsilon_x^2$ prior to the buckling. For graphite [Fig. 1 (b)], it gives a value of 980 GPa that is close to the experimental result 1060 GPa (Kelly, 1981). Results for the virtual graphites, *h*-BN, and virtual *h*-BN are shown in Table 3.

The shear modulus C_{44} was calculated using an in-house FORTRAN code. A simple shear deformation was applied to an A/B stacked 11-layers-graphene or *h*-BN (with periodic boundary conditions along the two directions of basal plane). That is, each layer is kept rigid and displaced with respect to each other in a direction parallel to the basal plane. The shear displacement is a linear function of the layer's position (out-of-plane direction) in the stack. Coordinates of the atoms in the sheared graphite were then fed into the in-house FORTRAN code that calculated LJ potential energy of the 6th layer with the same cut-off distance as used in the LAMMPS simulations. The magnitude of shear strains γ were selected to ensure the deformation is within a linear elastic region, *i.e.*, $-0.003 < \gamma < 0.003$. The obtained LJ potential energy of the graphene or *h*-BN layer in the middle of the stack exhibits a nearly perfect parabolic relation with respect to γ . For graphite, fitting the results using $U=1/2C_{44}\gamma^2$ yielded the shear modulus $C_{44}=0.3442$ GPa.

This value is significantly smaller than the experimental results: 4.3–4.5 GPa (Kelly, 1981; Tan, 2012a) and first-principles density functional theory (DFT) calculation results: 3.9–4.5 GPa (Mounet and Marzari, 2005). The book from Kelly (Kelly, 1981) has provided a review on elastic properties of graphite measured using different experimental techniques. They concluded that neutron scattering experiments gave the most reliable C_{44} value, 4.6 ± 0.2 GPa, because it is also consistent with the specific heat data. Recently Tan et al. (Tan, 2012b) used Raman spectroscopy to study the phonon properties of high quality few layer graphene flakes and concluded that the C_{44} is around 4.3 GPa, where structural defects should be minor. The DFT simulations were carried out for a perfect graphite crystal (Mounet and Marzari, 2005). Thus these experiments and first-principles calculations indicate that the reported and widely accepted C_{44} value ~ 4.5 GPa should arise from the intrinsic van der Waals interaction among graphene layers in bulk graphite. Our C_{44} result was also calculated for a perfect graphite crystal but using empirical force fields. In these force fields, the Lennard-Jones potential $U_{LJ}(r)=4\epsilon[(\sigma/r)^{12} - (\sigma/r)^6]$ is used to describe the interlayer van der Waals interactions. The two free parameters ϵ and σ were fitted to reproduce two experimental results: interlayer distance 3.4 Å and elastic modulus $C_{33}=36.5$ GPa in *z* direction. Thus the LJ force field often provides unsatisfactory predictions of other physical properties, *e.g.*, binding energy between graphene layers and cleavage energy of graphite (Gould et al., 2013; Lebègue et al., 2010; Liu et al., 2012; Sorella et al., 2009). We believe that the observed big difference of our calculated shear modulus C_{44} from other experiments and first-principles calculations should originate from the same reason. The C_{44} results for other materials are listed in Table 3 as well. Generally, the increasing of LJ potential parameter ϵ will significantly increase the interlayer shear modulus C_{44} .

3. Continuum mechanics model of intrinsic buckling strain

In this section, a continuum mechanics model is developed for the critical elastic buckling strain of a column made of the layered materials with a zero slenderness ratio and under a quasi-static loading. Here, the layered materials are modeled as homogenous mediums with hexagonal crystal symmetry (*i.e.*, transversely isotropic elastic). This is because graphite and *h*-BN have such crystal symmetry. Theoretical model for a more general case – orthorhombic symmetry – is presented in Appendix. Fig. 1(b) depicts our coordinate system, in which the basal planes of the crystal layers are parallel to the *x*–*y* plane. The origin point is placed in the center of the column and the *y*–*z* plane overlaps with the middle cross-section plane. A periodic boundary condition is applied in the lateral direction (*z*-axis), yielding $\rho \rightarrow \infty$ and thus $L/\rho=0$. This system is modeled as a plane-strain problem (in the *x*–*z* plane), aiming to be consistent with some popular experimental setups, *i.e.*, utilizing strain mismatch between a film made of layered crystalline materials and a pre-stretched substrate to drive the elastic buckling (Bowden et al., 1998; Efimenko et al., 2005; Kim et al., 2011; Koo et al., 2010; Zang et al., 2013) or bending induced periodic stripe/kinking microstructures during mechanical peeling of graphite flakes (Liu et al., 2010). Given that the *z*-axis in our model is the vertical direction of the film/substrate system in experiments, a compressive strain (via release of the pre-stretch deformation of substrate) is applied along the basal plane direction (*x*-axis). Under the constraint from the substrate, deformation in *y* direction is negligible, leading to the plane-strain condition.

For the column model shown in Fig. 1(b), we use the tensor index notation $x_1=x$, $x_2=y$, $x_3=z$. Thus, the displacement (u_i) and stress (σ_{ij}) boundary conditions are

$$\begin{aligned}
u_1|_{x=L/2} &= -\delta/2, \quad \sigma_{12}|_{x=L/2} = \sigma_{13}|_{x=L/2} = 0, \\
u_1|_{x=-L/2} &= \delta/2, \quad \sigma_{12}|_{x=-L/2} = \sigma_{13}|_{x=-L/2} = 0, \\
u_3|_{x=L/2} &= u_3|_{x=-L/2},
\end{aligned} \tag{1}$$

where δ is the relative displacement of the both ends moving toward each other. Note that the boundary conditions for displacements are consistent with those of the MD simulations, in which both ends are fixed. The displacement fields can be expressed as

$$u_1 = -\varepsilon x + \sum_{n=1}^N a_n \frac{L}{2n\pi} \sin \frac{2n\pi x}{L}, \quad u_2 = 0, \quad u_3 = \varepsilon b_0 z + \sum_{n=1}^N b_n \frac{L}{2n\pi} \cos \frac{2n\pi x}{L} \tag{2}$$

where $\varepsilon = \delta/L$ represents the homogeneous compressive strain in the x -direction prior to elastic buckling. Clearly, u_1 is an odd function of coordinate x . Thus, a series composed of sine functions is used to represent the displacement after the elastic buckling. Note that u_1 is independent of z because of the periodic boundary condition in the z direction. The displacement u_2 is set as zero to be consistent to the plane strain condition discussed early. The displacement u_3 is an even function of coordinate x . It is thus expressed as a series made of cosine functions. The first term of u_3 accounts for the lateral expansion in the z -direction. The periodic boundary condition suggests such a lateral expansion should be uniform. Hence the first term is expressed as a linear function of the coordinate z . It is also natural to assume the lateral expansion linearly depends on the applied compressive strain ε along the x -direction. The coefficient b_0 should be taken as a parameter that represents different types of boundary conditions in the z -direction. In our MD simulations, the lateral expansion is fixed. Therefore, the coefficient $b_0 = 0$. In the case of a freely relaxed boundary condition in z direction, b_0 should be equal to $b_0 = C_{13}/C_{33}$.

These displacement fields [Eq. (2)] satisfy the boundary conditions [Eq. (1)], with undetermined coefficients a_n and b_n . Only when the load is above the critical buckling value δ_{cr} , the a_n and b_n will have nonzero solutions.

Deformation gradient \mathbf{F} and the Green strain \mathbf{E} can be derived based on the displacement fields as

$$F_{11} = 1 + \frac{\partial u_1}{\partial x}, \quad F_{33} = 1 + \frac{\partial u_3}{\partial z}, \quad F_{13} = \frac{\partial u_1}{\partial z}, \quad F_{31} = \frac{\partial u_3}{\partial x}, \tag{3}$$

$$E_{11} = (F_{11}^2 + F_{31}^2 - 1)/2, \quad E_{33} = (F_{33}^2 + F_{13}^2 - 1)/2, \quad E_{13} = (F_{11}F_{13} + F_{31}F_{33})/2. \tag{4}$$

A hexagonal layered crystalline material has a transversely isotropic elasticity. In our model, since its basal plane is in the x - y plane, the constitutive law of linear elasticity can be expressed as

$$\begin{pmatrix} \sigma_{11} \\ \sigma_{22} \\ \sigma_{33} \\ \sigma_{23} \\ \sigma_{31} \\ \sigma_{12} \end{pmatrix} = \begin{pmatrix} C_{11} & C_{12} & C_{13} & 0 & 0 & 0 \\ C_{12} & C_{11} & C_{13} & 0 & 0 & 0 \\ C_{13} & C_{13} & C_{33} & 0 & 0 & 0 \\ 0 & 0 & 0 & C_{44} & 0 & 0 \\ 0 & 0 & 0 & 0 & C_{44} & 0 \\ 0 & 0 & 0 & 0 & 0 & (C_{11} - C_{12})/2 \end{pmatrix} \begin{pmatrix} \varepsilon_{11} \\ \varepsilon_{22} \\ \varepsilon_{33} \\ 2\varepsilon_{23} \\ 2\varepsilon_{31} \\ 2\varepsilon_{12} \end{pmatrix} \tag{5}$$

where C_{ij} are the stiffness constants. For investigating instability problem, we use the Green strain E_{ij} instead of the infinitesimal strain ε_{ij} in order to take account nonlinearity and consequently we use the second Piola-Kirchhoff stress, T_{ij} , instead of the conventional stress σ_{ij} . Substituting Eq. (4) into Eq. (5) yields

$$T_{11} = C_{11}E_{11} + C_{13}E_{33}, \quad T_{33} = C_{13}E_{11} + C_{33}E_{33}, \quad T_{13} = 2C_{44}E_{13}. \tag{6}$$

Then the strain energy density U is

$$U = 1/2(T_{11}E_{11} + 2T_{13}E_{13} + T_{33}E_{33}). \tag{7}$$

Integrating the energy density U in the column leads to the potential energy as

$$W = \frac{1}{L} \int_{-L/2}^{L/2} U dx, \tag{8}$$

in which a unit length is taken along the y and z directions, owing to the plane strain condition and the periodic boundary condition, respectively.

Following the principle of minimum total potential energy, partial derivatives of W with respect to the undetermined coefficients a_n and b_n should be equal to zero. Thus,

$$\begin{aligned}
g_1 = \partial \mathbf{W} / \partial b_1 &= b_1 (C_{44} - (G_{11} - 2C_{44}b_0 - G_{13}b_0)\epsilon) / 2 + O(b_1 (G_{11} + G_{13}b_0^2 + 2C_{44}b_0^2)\epsilon^2 / 4) = 0 \\
g_2 = \partial \mathbf{W} / \partial b_2 &= b_2 (C_{44} - (G_{11} - 2C_{44}b_0 - G_{13}b_0)\epsilon) / 2 + O(b_2 (G_{11} + G_{13}b_0^2 + 2C_{44}b_0^2)\epsilon^2 / 4) = 0 \\
f_1 = \partial \mathbf{W} / \partial a_1 &= a_1 (G_{11} - (3G_{11} - b_0G_{13})\epsilon) / 2 + O(a_1 (3G_{11} + G_{13}b_0^2)\epsilon^2 / 4) = 0 \\
..... \\
f_2 = \partial \mathbf{W} / \partial a_2 &= a_2 (G_{11} - (3G_{11} - b_0G_{13})\epsilon) / 2 + O(a_2 (3G_{11} + G_{13}b_0^2)\epsilon^2 / 4) = 0 \\
.....
\end{aligned} \tag{9}$$

where the quadratic and higher order terms of strain ϵ are omitted. Note that derivatives with respect to b_n ($n=1, 2, \dots$) always yield the same equation as

$$C_{44} - (G_{11} - 2C_{44}b_0 - G_{13}b_0)\epsilon = 0. \tag{10}$$

The derivatives with respect to a_n ($n=1, 2, \dots$) lead to another equation as

$$G_{11} - (3G_{11} - b_0G_{13})\epsilon = 0. \tag{11}$$

From Eqs. (10) or (11), we obtained the critical strain as

$$\epsilon_{cr}^{IBS} = \frac{C_{44}}{G_{11} - (2C_{44} + G_{13})b_0}, \tag{12}$$

or

$$\epsilon_{cr}^{IBS} = \frac{G_{11}}{3G_{11} - G_{13}b_0}. \tag{13}$$

In our homogeneous continuum mechanics model, the displacement fields are expressed as infinite series that satisfy the boundary conditions, so that the solution Eq. (12) or Eq. (13) is the exact solution of the intrinsic buckling strain of the layered materials without slenderness. Note that Eq. (12) was firstly reported in the PhD thesis of one of the authors (Liu, 2002).

The prediction from Eqs. (12) or (13) is valid only if the magnitude of ϵ_{cr} is small. Otherwise the higher order terms cannot be neglected in Eq. (9). From the aspect of physics, the adopted linear elasticity model may not be valid in the case of finite deformation. More importantly, only when the predicted ϵ_{cr} is lower than the material's elastic limit strain, the mechanical buckling could take place. Since Eq. (13) predicts a critical buckling strain $\epsilon_{cr} > 1/3$, its prediction should not be considered reliable.

It is interesting to notice that the Eq. (12) only includes the elastic constants of materials without any structural dimensions suggesting that such a mechanical buckling is an intrinsic property of materials. It is reasonable to understand this feature because in the case of $L/\rho=0$, the column [Fig. 1(a)] is inherently "structure-less". Here we define the critical buckling strain at $L/\rho=0$ [Eq. (12)] as the intrinsic buckling strain (IBS) ϵ_{cr}^{IBS} . The parameter n in displacement fields [Eq. (2)] represents different buckling modes. Interestingly, all the buckling modes share one degenerate eigenvalue, i.e., the ϵ_{cr}^{IBS} in Eq. (12).

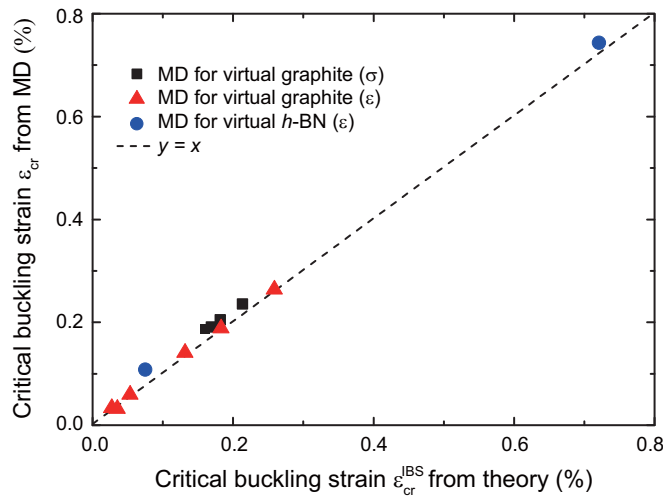


Fig. 4. A comparison of the intrinsic buckling strain ϵ_{cr}^{IBS} [Eq. (12) by setting $b_0=0$] with those converged ϵ_{cr} results from MD simulations. Each symbol represents one type of hexagonal layered crystalline materials simulated in Section 2.

Table 4

Elastic constants, continuum mechanics model predictions of the ϵ_{cr}^{IBS} [Eq. (12) or Eq. (13) with $b_0=C_{13}/C_{33}$] of selected hexagonal layered crystalline materials with a high degree of elastic anisotropy. Most of the materials are adopted from Table 1 in reference (Wang and Zheng, 2007). Elastic constants of *h*-BN are from reference (Duclaux et al., 1992). Elastic constants of WS₂ are from reference (Volkova et al., 2012).

Materials	C_{11}	C_{12}	C_{13}	C_{33}	C_{44}	Continuum mechanics prediction
Graphite (C)	1060	180	15	36.5	4.5	0.0043
Molybdenum sulfide (MoS ₂)	238	−54	23	51	18.6	0.0882
Biotite [K(Mg,Fe) ₃ AlSi ₃ O ₁₀ (OH,F) ₂]	186	32	12	54	5.8	0.0321
Phlogopite [KMg ₃ AlSi ₃ O ₁₀ (OH,F) ₂], B	178	30	15	51	6.5	0.0383
Phlogopite [KMg ₃ AlSi ₃ O ₁₀ (OH,F) ₂], A	179	32	26	51.7	5.6	0.0349
Muscovite [KAl ₂ Si ₃ O ₁₀ (OH,F) ₂]	178	42.4	14.5	54.9	12.2	0.0727
Gallium sulfide (peizoele) (GaS)	126.5	35.7	14.3	41.6	12	0.1059
Gallium selenide (peizoele) (GaSe)	106.4	30	12.1	35.8	10.2	0.1069
Rubidium nickel chloride (RbNiCl ₃)	35.2	10.0	22	72.2	2.5	0.0927
Indium selenide (InSe)	118.1	47.5	32	38.2	11.7	0.3606
Hexagonal Boron Nitride (<i>h</i> -BN)	750	150	−	18.7	2.52	0.0034
Tungsten sulfide (WS ₂)	236	61	8	42	12	0.0522

The value of ϵ_{cr}^{IBS} for graphite is plotted in Fig. 2 (the dashed line) to compare with MD simulation results using the AIREBO force field. The value of b_0 should be zero to be consistent with the boundary conditions in MD simulations, as discussed before. Thus we obtain the IBS $\epsilon_{cr}^{IBS} = C_{44}/C_{11} = 0.34416/980 = 0.03512\%$, in which the C_{11} modulus and C_{44} modulus are the values calculated in Section 2. Fig. 2 shows that the theoretical IBS agrees with the converged ϵ_{cr} from MD simulations very well (for $L \geq 20$ nm and under a loading velocity lower than 10^{-4} Å/ps). The theoretical ϵ_{cr}^{IBS} values are also compared with MD simulation results for graphite, *h*-BN, *virtual* graphite, and *virtual h*-BN (with Tersoff and LJ force fields) in Fig. 3. For each case, the predicted ϵ_{cr}^{IBS} agrees well with the converged ϵ_{cr} result in MD simulations. A detailed comparison is summarized in Table 3 and Fig. 4. We can, therefore, conclude that the IBS model accurately describes the critical elastic buckling strain of the studied layered crystalline materials at a zero slenderness ratio, at a sufficiently large length scale L , under a quasi-static loading condition.

Prior to ending this section, the theoretical IBS results under the freely relaxed side boundary condition ($b_0=C_{13}/C_{33}$) of a list of hexagonal layered crystalline materials are calculated and shown in Table 4. These materials are selected based on a thorough survey done by Wang and Zheng for hexagonal crystal materials with an extreme elastic anisotropy degree (Wang and Zheng, 2007). Owing to the intrinsic layered atomic structures, most of the hexagonal layered crystalline materials have an in-plane elastic constant C_{11} much larger than other elastic constants, particularly the shear modulus C_{44} . Thus, Eq. (12) often yields a smaller value of ϵ_{cr}^{IBS} than that of Eq. (13), with only one exception in the materials that we visited, InSe, for which Eq. (13) leads to a smaller value. However, this predicted ϵ_{cr}^{IBS} appears to be much higher than its material's yield strain and thus the elastic buckling is practically impossible. It is listed here just for theoretical interests. For those layered materials that attract enormous attentions at present, such as graphite, *h*-BN, MoS₂, and WS₂, their ϵ_{cr}^{IBS} results are smaller than 15%. It is thus feasible to manipulate morphologies of these layered materials via the intrinsic buckling mode and thus tune their physical properties in experiments for novel applications. It should be noted that elastic constants in Table 4 are from experiments. For graphite and *h*-BN, the results are different from Table 3.

We note that critical strain ϵ_{cr}^{IBS} predicted in Eq. (12) becomes $\epsilon_{cr}^{IBS} = (1 - \nu)/(1 - 2\nu)$ for isotropic materials, where ν is the Poisson's ratio. Because of the thermodynamics restriction: $-1 \leq \nu \leq 1/2$, this critical value of strain would exceed elastic limit strains for most real materials, and therefore is impractical.

There are many interesting layered crystalline materials that have other types of crystal symmetry (Geim and Grigorieva, 2013). For example, the perovskite-type material LaNb₂O₇, (Ca,Sr)₂Nb₃O₁₀, Bi₄Ti₃O₁₂ and Ca₂Ta₂TiO₁₀ have an orthorhombic symmetry. Thus a continuum mechanics model for an orthorhombic crystalline material is presented in Appendix. Note that for this symmetry, the column could undergo a mechanical buckling in either of the two lateral directions [i.e., *y* or *z*-axis in Fig. 1(b)], in comparison with only one direction (i.e., *z*-axis) for the hexagonal crystalline materials. Consequently, there is one more result for the ϵ_{cr}^{IBS} . Please refer to Appendix for details.

4. Size effect of the critical buckling strain

Fig. 2 and Fig. 3 demonstrate a significant size effect for the critical buckling strain of a column with length L smaller than 20 nm (meanwhile the slenderness ratio equals to zero). Indeed, for a graphite column length L reducing from 20 nm to 2 nm, the magnitude of ϵ_{cr} increases from 0.03343% to 0.4635%, i.e., more than 10 times increase. The continuum theoretical model presented in Section 3 cannot explain this size-dependent phenomenon. In this section, we will extend the continuum model in Section 3 to explain the observed size effect.

Careful analysis of the atomistic structures of the buckled layered crystalline materials reveals five types of deformation modes: (1) stretch/compression of the chemical bonds and (2) change of bond angles in the layer plane, (3) interlayer compression, (4) interlayer shear, and (5) bending of the dihedral bond angles out of the layer plane. In our continuum

mechanics model for a homogeneous media (Section 3), the strain term E_{11} can describe deformation modes (1) and (2), the E_{33} term accounts for mode (3), and the E_{13} term corresponds to mode (4). It appears that the mode (5), i.e., the out-of-plane bending of each atomically thin layer, is not considered. Previous studies showed that the mechanical strain energy arising from the bending of atomically thin materials generally follows $U \sim \frac{1}{2} D_b \kappa^2$, where D_b is the bending stiffness and κ is the curvature. For a bulk layered crystalline material, this energy term is negligible for two reasons. First, the value of D_b is normally very small. Second, the deformation of a column under compression at a large size scale yields a small κ value. However, when L value reduces down to nanometer range, the κ value in the buckled structure becomes more significant. The bending energy term, which accounts for the mode (5), should not be omitted anymore. It should be noted that the above bending energy term should be distinguished from the bending energy in the classic Euler or Timoshenko beam model, in which the bending effect arises from the stretch and compression on the opposite sides of a beam. We believe this is an inherent limitation of using classic continuum mechanics theory to describe the deformation of the layered crystalline materials at nanometer scale.

Then we add the bending energy term to Eq. (8):

$$W = \frac{1}{L} \int_{-L/2}^{L/2} U dx + \frac{1}{hL} \int_{-L/2}^{L/2} \frac{1}{2} D_b \kappa^2 dx, \quad (14)$$

where h is interlayer space of the layered materials. The curvature can be approximated as $\kappa = \frac{\partial^2 u_3}{\partial x^2}$.

Based on the displacement fields in Eq. (2), the curvature can be expressed as

$$\kappa = - \sum_{n=1}^N b_n \frac{2n\pi}{L} \cos \frac{2n\pi x}{L}. \quad (15)$$

The equilibrium state requires that the partial derivatives of W with respect to the undetermined coefficients a_n and b_n should be equal to zero. Thus,

$$\begin{aligned} g_1 = \partial W / \partial b_1 &= b_1 \left(C_{44} - (C_{11} - 2C_{44}b_0 - C_{13}b_0)\epsilon + \frac{D_b(2\pi)^2}{hL^2} \right) \\ &+ O(b_1(C_{11} + C_{13}b_0^2 + 2C_{44}b_0^2)\epsilon^2/4) = 0 \\ g_2 = \partial W / \partial b_2 &= b_2 \left(C_{44} - (C_{11} - 2C_{44}b_0 - C_{13}b_0)\epsilon + \frac{D_b(4\pi)^2}{hL^2} \right) \\ &+ O(b_2(C_{11} + C_{13}b_0^2 + 2C_{44}b_0^2)\epsilon^2/4) = 0 \\ &\dots\dots\dots \\ f_1 = \partial W / \partial a_1 &= a_1(C_{11} - (3C_{11} - b_0C_{13})\epsilon)/2 + O(a_1(3C_{11} + C_{13}b_0^2)\epsilon^2/4) = 0 \\ f_2 = \partial W / \partial a_2 &= a_2(C_{11} - (3C_{11} - b_0C_{13})\epsilon)/2 + O(a_2(3C_{11} + C_{13}b_0^2)\epsilon^2/4) = 0 \\ &\dots\dots\dots \end{aligned} \quad (16)$$

Note that adding the bending energy term in Eq. (14) leads to an extra term $\frac{D_b(2n\pi)^2}{hL^2}$ in Eq. (16) compared with Eq. (9). The critical buckling strain now becomes

Table 5

The bending stiffness D_b , the equilibrium interlayer distance h , and the calculated length parameter l_0 of h -BN, graphite and virtual graphite are summarized.

LJ parameter	D_b (eV)	h (nm)	l_0 (nm)
Graphite ^a	1.46 ^c	0.3369	8.918
Graphite (ϵ , σ) ^b		0.336	9.08
Virtual Graphite (2ϵ , σ) ^b		0.336	6.414
Virtual Graphite (5ϵ , σ) ^b		0.336	4.046
Virtual Graphite (7ϵ , σ) ^b		0.336	3.413
Virtual Graphite (10ϵ , σ) ^b		0.336	2.848
Virtual Graphite (10ϵ , 1.1σ) ^b		0.3691	3.119
Virtual Graphite (10ϵ , 1.2σ) ^b		0.4031	3.367
Virtual Graphite (10ϵ , 1.3σ) ^b		0.4372	3.473
Virtual Graphite (10ϵ , 1.4σ) ^b		0.4712	3.554
h -BN ^b	1.29 ^c	0.3357	6.23

^a Modeled by AIREBO force field (Stuart et al., 2000).

^b Modeled by Tersoff and LJ potentials (Kinaci et al., 2012; Tersoff, 1989).

^c Calculated using modified Tersoff potential for h -BN (Kinaci et al., 2012; Singh et al., 2013).

$$\varepsilon_{cr} = \frac{C_{44}}{C_{11} - 2(C_{44} + C_{13})b_0} + \frac{D_b}{(C_{11} - 2(C_{44} + C_{13})b_0)h} \left(\frac{2n\pi}{L} \right)^2. \quad (17)$$

By defining a length parameter $l_0 = 2\pi\sqrt{D_b/C_{44}h}$, the Eq. (17) can be written as

$$\begin{aligned} \varepsilon_{cr} &= \left[1 + \left(n \frac{l_0}{L} \right)^2 \right] \frac{C_{44}}{C_{11} - 2(C_{44} + C_{13})b_0} \\ &= \left[1 + \left(n \frac{l_0}{L} \right)^2 \right] \varepsilon_{cr}^{IBS} \end{aligned} \quad (18)$$

The difference between Eq. (18) and the IBS critical buckling strain in Eq. (12) is a geometry dependent pre-factor, where the size effect clearly manifests itself. For a large L value, Eq. (18) reduces to the ε_{cr}^{IBS} in Eq. (12). Reducing the column length L leads to an enhancement of the critical buckling strain. In addition, Eq. (18) shows that the different buckling modes n do not share a degenerated critical buckling strain value any more.

For the graphite column (AIREBO force field) in Section 2, we have the parameters $D_b = 1.46$ eV (Singh et al., 2013), $C_{44} = 0.3442$ GPa, $h = 0.3369$ nm. Thus the l_0 can be calculated as 8.9 nm. The theoretical model [Eq. (18)], shown as the solid black line in Fig. 3, is compared with MD simulation results. The agreement is very good. For the cases of h -BN, graphite (Tersoff and LJ potentials), and *virtual* graphite, Table 5 lists the bending stiffness D_b results, the equilibrium interlayer distance h , and the calculated length parameter l_0 . Fig. 3 compares the theoretical model Eq. (18) with MD simulations of these cases as well. The agreement is also good, indicating the bending of atomic layers as origin of the observed size effect. Overall the l_0 value is quite small, varying from 2–10 nm. Only when the column length L (i.e., buckling wavelength) close or below l_0 , the critical buckling strain will significantly deviates from the intrinsic buckling strain ε_{cr}^{IBS} .

5. Discussions

Before we draw conclusions, this section will provide some in-depth discussions and implications.

The mechanical buckling of anisotropic materials has been a topic of interests for a quite long time. The recent book from Bažant provides an excellent review on relevant topics (Bažant and Cedolin, 2010). Several different cases have been studied. The internal buckling happens for a continuum block/column under a uniaxial compression and being constrained by rigid and perfectly lubricated side edges (Biot, 1965). As the slenderness ratio approaching to zero, this case appears to be similar to our MD simulations. But it should be aware that previous models usually assumed the anisotropic materials to be incompressible. The incompressibility should inevitably bring the effects of the rigid side boundary to the buckling that happens in the internal part of the block. In order to directly compare with our theoretical model, we did some derivations of the Biot's original model (Biot, 1965). Indeed, the critical buckling strain ε_{cr} of such internal buckling, i.e., $4C_{44}/(3C_{11}-C_{13})$ is quite different from our model C_{44}/C_{11} that is derived from Eq. (12) in accordance to the fixed side boundary condition in MD. The second case studied previously is the buckling of a thick slab under a uniaxial compression with free side boundaries. But the materials were also assumed to be incompressible. As the slenderness ratio approaching to zero, Biot pointed out that it should coincide with the surface buckling of a semi-infinite half space, which clearly is different from our study. The third case is the buckling of a thick beam. As early as in 1889, Engesser proposed a model that took both the bending and shearing effect into account (Bažant and Cedolin, 2010). The critical buckling strain can be expressed as:

$$\varepsilon_{cr} = 4\pi^2 \left[\left(\frac{L}{\rho} \right)^2 + 4\pi^2 \frac{\eta Y}{G} \right]^{-1}, \quad (19)$$

where Y is Young's modulus of the column along longitudinal x direction. Here η is a factor related to the geometry of the cross-section (Timoshenko and Gere, 2012). It is usually taken 1.12 and 1.11 for rectangular and circular cross-sections, respectively. Taking the slenderness ratio L/ρ approaching zero in Eq. (19) leads to a critical strain $\varepsilon_{cr} = G/\eta Y$. It should be noted that the thick beam can deform in the transverse direction under the uniaxial compression, which is analogous to the freely relaxed side boundary condition we discussed in Section 3, i.e., $b_0 = C_{13}/C_{33}$. The clear difference can be easily understood since a beam theory was used in Engesser's model that is not appropriate for a very thick three-dimension block. More importantly, it should be aware that previous homogeneous continuum mechanical models cannot explain the size effect, which is observed in our MD simulations and has been successfully explained using our model.

It is worth noting that our homogeneous continuum mechanical model Eq. (12) embodies neither an intrinsic length scale nor internal atomistic microstructures. The graphite column is simply described as a homogeneous continuum bulk. The IBS agrees very well with those determined by MD simulations (down to 20 nm). This excellent agreement suggests that the critical buckling point of a thick graphite column (\sim zero slenderness ratio) above tens of nanometer scale is governed by its macroscopic elastic properties. This should be true for other hexagonal layered crystalline materials (Table 4). This conclusion is also consistent with previous studies of multi-walled carbon nanotubes (Liu et al., 2001; 2003), which modeled the multi-walled carbon nanotube (MWCNT) as a homogeneous continuum beam and successfully explained the

rippling in MWCNT under bending in experiments (Poncharal et al., 1999). It should be noted that to model the post-buckling of the layered crystalline materials, such as the formation of kinking band, we may still require atomistic simulations (Li et al., 2007; Liu et al., 2011), thin shell/plate FEA models (Liu et al., 2005), or those atomistic-based FEA techniques (Arroyo and Belytschko, 2003).

From our homogeneous continuum mechanics model, we can conclude that the drastically low interlayer shear modulus C_{44} in comparison with the in-plane modulus C_{11} is the origin for the observed profound shear mode of instability and the anomalous elastic buckling of a column with an infinitesimal slenderness ratio. For a crystal material, the concept of elastic anisotropy degree $\delta(\mathbf{C})$ is often adopted to quantify the difference of elastic modulus along different crystalline directions (Nye, 1985; Wang and Zheng, 2007). The special crystal structure of a layered material implies a high $\delta(\mathbf{C})$. Indeed, among the top 20 hexagonal crystal materials with a high $\delta(\mathbf{C})$, most of them are layered crystalline materials (Wang and Zheng, 2007). It is natural to expect that a high elastic anisotropy degree $\delta(\mathbf{C})$ should lead to a small IBS $\varepsilon_{\text{cr}}^{\text{IBS}}$. However, a comparison between the IBS ε_{cr} results and the anisotropy degree shows several exceptions. For instance, in Table 4, MoS₂, Muscovite [KAl₂Si₃O₁₀(OH,F)₂], or Rubidium nickel chloride (RbNiCl₃) has a similar IBS ε_{cr} , i.e., 0.1583, 0.1622, and 0.1552, but they show a significant difference in $\delta(\mathbf{C})$, i.e., 0.608, 0.5, and 0.408. Another example is that although Muscovite [KAl₂Si₃O₁₀(OH,F)₂] has a larger $\delta(\mathbf{C})$ in comparison with Biotite [K(Mg,Fe)₃AlSi₃O₁₀(OH,F)₂], i.e., 0.608 vs. 0.557, its IBS ε_{cr} result is much higher as well, i.e., 0.1583 vs. 0.0643. Here we propose that the $\varepsilon_{\text{cr}}^{\text{IBS}}$ [Eq. (12)] under the freely relaxed side boundary condition ($b_0 = C_{13}/C_{33}$) could serve as an alternative measure to characterize the degree of elastic anisotropy for hexagonal crystal materials. In the same spirit, Eqs. (A13) and (A14) could be used to measure the degree of elastic anisotropy for orthorhombic crystalline materials. One clear advantage is that such a measure has a clearer physical meaning.

In light of the very weak interlayer physical interactions, it is intuitively reasonable to approximate the critical buckling stress/strain of a multi-layered stack by that of a mono-crystal-layer (Guo et al., 2011). Our study shows that such an approximation is problematic. For example, based on Euler model, for a graphene layer with length $L=20, 30$, or 40 nm, the ε_{cr} is 0.00358%, 0.00159%, and 0.000896% given the thickness of graphene monolayer as 0.066 nm (Wang et al., 2005; Yakobson et al., 1996). But in our MD simulations for a multi-layer stack, they share a similar $\varepsilon_{\text{cr}}=0.0351\%$. It clearly shows that despite its small magnitude, the interlayer modulus C_{44} plays a decisive role in determining the mechanical buckling of a multi-layered stack of graphenes.

Employing elastic buckling to tune the physical properties of layered crystalline materials has several clear advantages. First, there are no chemical or physical damages to the crystal integrity. It could avoid some undesired side effects that often occur when tailoring the physical properties via methods such as cutting, chemical or physical adsorptions. Second, in principle, the elastic buckling is recoverable. That means utilizing buckling under a cyclic loading/unloading condition can repeatedly control the material morphologies and thus their properties. This is highly desirable in nanotechnology, which can enable many new applications, such as the mechanical sensor, and the responsive materials.

Making use of the shear mode of instability has several more advantages. First, a layered crystalline material can undergo a mechanical buckling with a very low slenderness ratio ($L/\rho \sim 0$), suggesting that the buckling wavelength L can be tuned to a very small value. Our MD simulations demonstrate the scale of L down to ~ 20 nm. It can be used to generate periodic surface structures at a nanometer scale, which is a difficult task by employing the bending mode of instability. Second, a distinctive kinking morphology is the signature of the shear mode instability at post-buckling stage (Budiansky et al., 1998; Liu et al., 2010). In the kink, there is a sharp transition corner connecting two consecutive straight segments, which is potentially useful in some novel applications. For example, an electric current in graphene nano-bubbles can generate a giant pseudo-magnetic field (Levy et al., 2010). It was found that strength of the magnetic field depended on a change of curvature. The sharp corners in the kinks could be used to design nano-devices that can generate dynamically tunable giant pseudo-magnetic fields. Third, under the shear mode of instability, there are no strains in the basal planes of the layered crystalline materials (only shear deformation occurs among adjacent crystal layers). This could be another benefit, if the atomistic structure of crystal layers would like to be conserved.

6. Summary

In this paper, we study the elastic buckling of a column made of layered crystalline materials being subject to a uniaxial compressive load along the basal plane direction, using MD simulations and continuum mechanics modeling. In our MD simulations for graphite, *h*-BN, *virtual* graphite, and *virtual h*-BN, we found that the columns (at a zero slenderness ratio due to periodic boundary condition) had a constant critical buckling strain value given that the length L is higher than certain values. Our continuum mechanics model reveals that such a converged critical buckling strain solely depends on the material's elastic constants (without structural dimensions), implying that it is an intrinsic material property. A new concept, intrinsic buckling strain (IBS), is thus defined. For a set of typical layered crystalline materials, the $\varepsilon_{\text{cr}}^{\text{IBS}}$ is much lower than elastic limit stain of the materials, indicating the mechanical buckling occurs prior to the failure of the materials. Our results also reveal that a high degree of elastic anisotropy is the origin for the anomalous mechanical buckling in the absence of structural slenderness.

In MD simulations, reducing the length L leads to a gradual increase of ε_{cr} , deviating from the constant $\varepsilon_{\text{cr}}^{\text{IBS}}$. We introduced a bending energy term, which describes the bending deformation of each individual atomic layer, in the continuum mechanics model. The good agreement between our continuum model [Eq. (18)] and the MD simulations indicates

that the bending deformation of atomic layers is the origin for the observed size effect. A characteristic length parameter l_0 is defined, which is an intrinsic material parameter. When the column length L is comparable or smaller than l_0 , the size effect on ε_{cr} shows up.

Besides the layered crystalline materials, some biomaterials (e.g. nacre, shell, bone, etc.), fiber reinforce composites, or geological strata also have the similar microstructures and high elastic anisotropy. Our studies could provide some insights to understand their mechanical buckling behavior. In the end, some in-depth discussions and potential applications in nanotechnology are provided. This study could provide guidelines for engineering layered crystalline materials in various nano-materials and nano-devices via mechanical buckling.

Acknowledgment

J. Z. Liu acknowledges the support of a seed grant from the Engineering Faculty at Monash University and acknowledges National Computational Infrastructure at Australian National University and Monash Sun Grid High-Performance Computing Facility at Monash University for providing the computational resource. Y.L. acknowledges the financial support from NSFC through Grant no. 11302163 and 11321062. L. Wang acknowledges the support from the National Science Foundation (USA) and Q. S. Z. acknowledges the financial support from NSFC through Grant no. 10832005, the National Basic Research Program of China (Grant no. 2007CB936803), and the National 863 Project (Grant no. 2008AA03Z302).

Appendix. Continuum mechanics model for intrinsic buckling strain of orthorhombic crystalline materials

A continuum mechanics model is detailed here for a column made of orthorhombic crystalline materials [Fig. 1(b)]. The mechanical buckling could occur in either of the two lateral directions. Thus periodic boundary conditions are applied in both y and z directions. Similar to the previous derivations in Section 3, boundary conditions are

$$\begin{aligned} u_1|_{x=L/2} &= -\delta/2, & \tau_{12}|_{x=L/2} &= 0, & \tau_{13}|_{x=L/2} &= 0, \\ u_1|_{x=-L/2} &= \delta/2, & \tau_{12}|_{x=-L/2} &= 0, & \tau_{13}|_{x=-L/2} &= 0, \\ u_2|_{x=-L/2} &= u_2|_{x=L/2}, & u_3|_{x=-L/2} &= u_3|_{x=L/2}, \end{aligned} \quad (A1)$$

where δ is the relative displacement of the both ends moving toward each other. The displacement fields can be expressed as

$$u_1 = -\varepsilon x + \sum_{n=1}^N a_n \frac{L}{2n\pi} \sin \frac{2n\pi x}{L}, \quad u_2 = \varepsilon k_0 y + \sum_{n=1}^N k_n \frac{L}{2n\pi} \cos \frac{2n\pi x}{L}, \quad u_3 = \varepsilon b_0 z + \sum_{n=1}^N b_n \frac{L}{2n\pi} \cos \frac{2n\pi x}{L}, \quad (A2)$$

where $\varepsilon = \delta/L$ represents the homogeneous compressive strain in x -direction prior to elastic buckling. Note that u_2 has a different expression compared to the transverse isotropic materials, e.g., hexagonal crystalline materials. The first terms of u_2 and u_3 are adopted to account for the different types of side boundary conditions in z and y directions, respectively. A fixed side boundary condition, as used in our MD simulations for graphite etc., means k_0 and b_0 equal to zero, whereas the freely relaxed side boundary condition requires $k_0 = C_{12}/C_{22}$ and $b_0 = C_{13}/C_{33}$ in which C_{12} , C_{13} , C_{22} and C_{33} are elastic constants. These displacement fields [Eq. (A2)] satisfy the boundary conditions [Eq. (A1)]. Parameters a_n , k_n and b_n are unknown coefficients. Only when the load is above the critical buckling value δ_{cr} , the a_n , k_n and b_n will have nonzero solutions.

Deformation gradient \mathbf{F} and the first Seth strain \mathbf{E} can be derived based on the displacement fields as

$$\begin{aligned} F_{11} &= 1 + \frac{\partial u_1}{\partial x}, & F_{22} &= 1 + \frac{\partial u_2}{\partial y}, & F_{33} &= 1 + \frac{\partial u_3}{\partial z}, \\ F_{12} &= \frac{\partial u_1}{\partial y}, & F_{13} &= \frac{\partial u_1}{\partial z}, & F_{23} &= \frac{\partial u_2}{\partial z}, \\ F_{21} &= \frac{\partial u_2}{\partial x}, & F_{31} &= \frac{\partial u_3}{\partial x}, & F_{32} &= \frac{\partial u_3}{\partial y}, \end{aligned} \quad (A3)$$

$$E_{11} = (F_{11}^2 + F_{21}^2 + F_{31}^2 - 1)/2, \quad E_{22} = (F_{12}^2 + F_{22}^2 + F_{32}^2 - 1)/2, \quad E_{33} = (F_{13}^2 + F_{23}^2 + F_{33}^2 - 1)/2$$

$$E_{12} = E_{21} = (F_{11}F_{12} + F_{21}F_{22} + F_{31}F_{32})/2, \quad E_{13} = E_{31} = (F_{11}F_{13} + F_{21}F_{23} + F_{31}F_{33})/2,$$

$$E_{23} = E_{32} = (F_{12}F_{13} + F_{22}F_{23} + F_{32}F_{33})/2. \quad (A4)$$

For an orthorhombic crystalline material, the constitutive law of linear elasticity can be expressed as

$$\begin{pmatrix} \sigma_{11} \\ \sigma_{22} \\ \sigma_{33} \\ \sigma_{23} \\ \sigma_{31} \\ \sigma_{12} \end{pmatrix} = \begin{pmatrix} C_{11} & C_{12} & C_{13} & 0 & 0 & 0 \\ C_{12} & C_{22} & C_{23} & 0 & 0 & 0 \\ C_{13} & C_{23} & C_{33} & 0 & 0 & 0 \\ 0 & 0 & 0 & C_{44} & 0 & 0 \\ 0 & 0 & 0 & 0 & C_{55} & 0 \\ 0 & 0 & 0 & 0 & 0 & C_{66} \end{pmatrix} \begin{pmatrix} \varepsilon_{11} \\ \varepsilon_{22} \\ \varepsilon_{33} \\ 2\varepsilon_{23} \\ 2\varepsilon_{31} \\ 2\varepsilon_{12} \end{pmatrix}, \quad (\text{A5})$$

where σ and τ represent the normal and shear stress components, ε and γ denote the normal and shear strain components, and C_{ij} are the stiffness constants. Substituting Eq. (A4) into Eq. (A5) yields the second Piola-Kirchhoff stress \mathbf{T} as

$$\begin{aligned} T_{11} &= C_{11}E_{11} + C_{12}E_{22} + C_{13}E_{33}, & T_{22} &= C_{12}E_{11} + C_{22}E_{22} + C_{23}E_{33}, \\ T_{33} &= C_{13}E_{11} + C_{23}E_{22} + C_{33}E_{33}, & T_{23} &= 2C_{44}E_{23}, & T_{13} &= 2C_{55}E_{13}, & T_{12} &= 2C_{66}E_{12}. \end{aligned} \quad (\text{A6})$$

Then the strain energy density U is

$$U = 1/2(T_{11}E_{11} + T_{22}E_{22} + T_{33}E_{33} + 2T_{13}E_{13} + 2T_{23}E_{23} + 2T_{12}E_{12}). \quad (\text{A7})$$

Integrating the energy density U in the column leads to the potential energy as

$$W = \frac{1}{L} \int_{-L/2}^{L/2} U dx, \quad (\text{A8})$$

in which unit lengths are taken along the y and z directions, owing to the periodic boundary conditions.

Following the principle of minimum total potential energy, partial derivatives of W with respect to the undetermined coefficients a_n , b_n , and k_n should be equal to zero. Thus,

$$\begin{aligned} g_1 &= \partial W / \partial b_1 = b_1(C_{55} - (C_{11} - 2C_{55}b_0 - C_{12}k_0 - C_{13}b_0)\varepsilon)/2 + O(\varepsilon^2) = 0 \\ g_2 &= \partial W / \partial b_2 = b_2(C_{55} - (C_{11} - 2C_{55}b_0 - C_{12}k_0 - C_{13}b_0)\varepsilon)/2 + O(\varepsilon^2) = 0 \\ &\dots \\ m_1 &= \partial W / \partial k_1 = k_1(C_{66} - (C_{11} - 2C_{66}k_0 - C_{12}k_0 - C_{13}b_0)\varepsilon)/2 + O(\varepsilon^2) = 0 \\ m_2 &= \partial W / \partial k_2 = k_2(C_{66} - (C_{11} - 2C_{66}k_0 - C_{12}k_0 - C_{13}b_0)\varepsilon)/2 + O(\varepsilon^2) = 0 \\ &\dots \\ f_1 &= \partial W / \partial a_1 = a_1(C_{11} - (3C_{11} - C_{12}k_0 - C_{13}b_0)\varepsilon)/2 + O(\varepsilon^2) = 0 \\ f_2 &= \partial W / \partial a_2 = a_2(C_{11} - (3C_{11} - C_{12}k_0 - C_{13}b_0)\varepsilon)/2 + O(\varepsilon^2) = 0 \\ &\dots \end{aligned} \quad (\text{A9})$$

where the quadratic and higher order terms of strain ε are omitted. Note that derivatives with respect to b_n ($n=1, 2, 3, 4 \dots$) always yield the same equation as

$$C_{55} - (C_{11} - 2C_{55}b_0 - C_{12}k_0 - C_{13}b_0)\varepsilon = 0. \quad (\text{A10})$$

The derivatives with respect to k_n ($n=1, 2, 3, 4 \dots$) lead to an equation as

$$C_{66} - (C_{11} - 2C_{66}k_0 - C_{12}k_0 - C_{13}b_0)\varepsilon = 0. \quad (\text{A11})$$

The derivatives with respect to a_n ($n=1, 2, 3, 4 \dots$) lead to an equation as

$$C_{11} - (3C_{11} - C_{12}k_0 - C_{13}b_0)\varepsilon = 0. \quad (\text{A12})$$

From Eq. (A10), (A11) or (A12), we obtained the IBS ε_{cr} as

$$\varepsilon_{cr} = \frac{C_{55}}{C_{11} - C_{12}k_0 - (2C_{55} + C_{13})b_0}, \quad (\text{A13})$$

or

$$\varepsilon_{cr} = \frac{C_{66}}{C_{11} - C_{13}b_0 - (2C_{66} + C_{12})k_0}, \quad (\text{A14})$$

or

$$\varepsilon_{cr} = \frac{C_{11}}{3C_{11} - C_{12}k_0 - C_{13}b_0}. \quad (A15)$$

Knowledge of the perovskite layered crystalline materials is quite limited (Geim and Grigorieva, 2013). A complete set of elastic constants for LaNb_2O_7 , $(\text{Ca},\text{Sr})_2\text{Nb}_3\text{O}_{10}$, $\text{Bi}_4\text{Ti}_3\text{O}_{12}$, $\text{Ca}_2\text{Ta}_2\text{TiO}_{10}$ are not available. Therefore, a quantitative comparison between the theoretical results Eq. (A13) and (A14) and numerical simulations are not feasible at present.

Note that Eq. (A13) and Eq. (A15) can be reduced into Eqs. (12) and (13) for the hexagonal crystalline materials, through letting $C_{22}=C_{11}$, $C_{23}=C_{13}$, and $C_{55}=C_{44}$ because of the hexagonal crystal symmetry and $k_0=0$ due to the plane-strain conditions adopted in Eqs. (12) and (13).

References

- Arroyo, M., Belytschko, T., 2003. Nonlinear Mechanical Response and Rippling of Thick Multiwalled Carbon Nanotubes. *Phys. Rev. Lett.* 91, 215505, <http://dx.doi.org/10.1103/PhysRevLett.91.215505>.
- Baowan, D., Hill, J.M., 2007. Nested boron nitride and carbon-boron nitride nanocones. *Micro Nano Lett.* 2, 46–49.
- Bazant, Z.P., Cedolin, L., 2010. *Stability of Structures*. World Scientific, Singapore.
- Biot, M.A., 1965. *Mechanics of Incremental Deformations*. John Wiley & Sons Ltd, New York.
- Biot, M.A., 1957. Folding Instability of a Layered Viscoelastic Medium under Compression. *Proceedings of the Royal Society A: Mathematical, Physical and Engineering Sciences*, vol. 242, pp. 444–454. doi:10.1098/rspa.1957.0187.
- Bowden, N., Brittain, S., Evans, A.G., Hutchinson, J.W., Whitesides, G.M., 1998. Spontaneous formation of ordered structures in thin films of metals supported on an elastomeric polymer. *Nature* 393, 146–149.
- Brau, F., Vandeparre, H., Sabbah, A., Poulard, C., Boudaoud, A., Damman, P., 2010. Multiple-length-scale elastic instability mimics parametric resonance of nonlinear oscillators. *Nat. Photo.* 7, 56–60, <http://dx.doi.org/10.1038/nphys1806>.
- Budd, C.J., Edmunds, R., Hunt, G.W., 2003. A nonlinear model for parallel folding with friction. *Proceedings of the Royal Society A: Mathematical, Physical and Engineering Sciences*, vol. 459, pp. 2097–2119. doi:10.1098/rspa.2003.1139.
- Budiansky, B., Fleck, N.A., Amazigo, J.C., 1998. On kink-band propagation in fiber composites. *J. Mech. Phys. Solids* 46, 1637–1653.
- Byskov, E., Christoffersen, J., Christensen, C.D., Poulsen, J.S., 2002. Kinkband formation in wood and fiber composites—morphology and analysis. *Int. J. Solids Struct.* 39, 3649–3673.
- Ci, L., Song, L., Jin, C., Jariwala, D., Wu, D., Li, Y., Srivastava, A., Wang, Z.F., Storr, K., Balicas, L., Liu, F., Ajayan, P.M., 2010. Atomic layers of hybridized boron nitride and graphene domains. *Nat. Mater.* 9, 430–435, <http://dx.doi.org/10.1038/nmat2711>.
- Ci, L., Xu, Z., Wang, L., Gao, W., Ding, F., Kelly, K., Yakobson, B., Ajayan, P., 2008. Controlled nanocutting of graphene. *Nano Res.* 1, 116–122.
- Cranford, S.W., 2013. Buckling induced delamination of graphene composites through hybrid molecular modeling. *Appl. Phys. Lett.* 102, 031902–031906, <http://dx.doi.org/10.1063/1.4788734>.
- Duclaux, L., Nysten, B., Issi, J.P., Moore, A.W., 1992. Structure and low-temperature thermal conductivity of pyrolytic boron nitride. *Phys. Rev. B* 46, 3362–3367, <http://dx.doi.org/10.1103/PhysRevB.46.3362>.
- Efimenko, K., Rackaitis, M., Manias, E., Vaziri, A., Mahadevan, L., Genzer, J., 2005. Nested self-similar wrinkling patterns in skins. *Nat. Mater.* 4, 293–297, <http://dx.doi.org/10.1038/nmat1342>.
- Elias, D.C., Nair, R.R., Mohiuddin, T., Morozov, S.V., 2009. Control of graphene's properties by reversible hydrogenation: evidence for graphane. *Science* 323, 610–613, <http://dx.doi.org/10.1126/science.1092905>.
- Geim, A., Novoselov, K., 2007. The rise of graphene. *Nat. Mater.* 6, 183–191.
- Geim, A.K., Grigorieva, I.V., 2013. Van der Waals heterostructures. *Nature* 499, 419–425, <http://dx.doi.org/10.1038/nature12385>.
- Gere, J.M., Timoshenko, S.P., 1998. *Mechanics of Materials*, 4th ed. Chapman and Hall, London.
- Ghosh, S., Arroyo, M., 2013. An atomistic-based foliation model for multilayer graphene materials and nanotubes. *J. Mech. Phys. Solids* <http://dx.doi.org/10.1016/j.jmps.2012.07.002>.
- Golberg, D., Bando, Y., Huang, Y., Terao, T., Mitome, M., 2010. Boron nitride nanotubes and nanosheets. *ACS Nano* 4, 2979–2993, <http://dx.doi.org/10.1038/nmat3542>.
- Gould, T., Liu, Z., Liu, J.Z., Dobson, J.F., Zheng, Q.-S., 2013. Binding and interlayer force in the near-contact region of two graphite slabs: experiment and theory. *J. Chem. Phys.* <http://dx.doi.org/10.1063/1.4839615>.
- Guo, F., Kim, F., Han, T.H., Shenoy, V.B., Huang, J., Hurt, R.H., 2011. Hydration-Responsive Folding and Unfolding in Graphene Oxide Liquid Crystal Phases. *ACS Nano* 5, 8019–8025, <http://dx.doi.org/10.1021/nn2025644>.
- Haigh, S.J., Gholinia, A., Jalil, R., Romani, S., Britnell, L., Elias, D.C., Novoselov, K.S., Ponomarenko, L.A., Geim, A.K., Gorbachev, R., 2012. Cross-sectional imaging of individual layers and buried interfaces of graphene-based heterostructures and superlattices. *Nat. Mater.* 11, 1–4, <http://dx.doi.org/10.1038/nmat3386>.
- Hohlfeld, E., Mahadevan, L., 2011. Unfolding the Sulcus. *Phys. Rev. Lett.* 106, 105702, <http://dx.doi.org/10.1103/PhysRevLett.106.105702>.
- Huang, Z.Y., Hong, W., Suo, Z., 2005. Nonlinear analyses of wrinkles in a film bonded to a compliant substrate. *J. Mech. Phys. Solids* 53, 2101–2118, <http://dx.doi.org/10.1016/j.jmps.2005.03.007>.
- Hunt, G.W., Peletier, M.A., Wade, M.A., 2000. The Maxwell stability criterion in pseudo-energy models of kink banding. *J. Struct. Geol.* 22, 669–681.
- Kelly, B.T., 1981. *Physics of Graphite*, 1st ed. Applied Science Publishers, London.
- Kim, D.H., Ahn, J.H., Choi, W.M., Kim, H.S., Kim, T.H., Song, J., 2008. Stretchable and foldable silicon integrated circuits. *Science* 320, 507–511, <http://dx.doi.org/10.1126/science.1078727>.
- Kim, J., Yoon, J., Hayward, R.C., 2009. Dynamic display of biomolecular patterns through an elastic creasing instability of stimuli-responsive hydrogels. *Nat. Mater.* 9, 159–164, <http://dx.doi.org/10.1038/nmat2606>.
- Kim, P., Abkarian, M., Stone, H.A., 2011. Hierarchical folding of elastic membranes under biaxial compressive stress. *Nat. Mater.* 10, 952–957, <http://dx.doi.org/10.1038/nmat3144>.
- Kim, R.H., Kim, D.H., Xiao, J., Kim, B.H., Park, S.I., Panilaitis, B., Ghaffari, R., Yao, J., Li, M., Liu, Z., Malyarchuk, V., Kim, D.G., Le, A.-P., Nuzzo, R.G., Kaplan, D.L., Omenetto, F.G., Huang, Y., Kang, Z., Rogers, J.A., 2010. Waterproof AlInGaP optoelectronics on stretchable substrates with applications in biomedicine and robotics. *Nat. Mater.* 9, 929–937, <http://dx.doi.org/10.1038/nmat2879>.
- Koo, W.H., Jeong, S.M., Araoka, F., Ishikawa, K., Nishimura, S., Toyooka, T., Takezoe, H., 2010. Light extraction from organic light-emitting diodes enhanced by spontaneously formed buckles. *Nat. Photo.* 4, 222–226, <http://dx.doi.org/10.1038/nphoton.2010.7>.
- Kyriakides, S., Arseculeratne, R., Perry, E.J., Liechti, K.M., 1995. On the compressive failure of fiber reinforced composites. *Int. J. Solids Struct.* 32, 689–738.
- Kinaci, A., Haskins, J.B., Sevik, C., Çağın, T., 2012. Thermal conductivity of BN-C nanostructures. *Phys. Rev. B* 86, 115410–115418, <http://dx.doi.org/10.1103/PhysRevB.86.115410>.

- Leahy, B.D., Pocivavsek, L., Meron, M., Lam, K.L., Salas, D., Viccaro, P.J., Lee, K.Y.C., Lin, B., 2010. Geometric Stability and Elastic Response of a Supported Nanoparticle Film. *Phys. Rev. Lett.* 105, 058301, <http://dx.doi.org/10.1103/PhysRevLett.105.058301>.
- Lebègue, S., Harl, J., Gould, T., Ángyán, J., Kresse, G., Dobson, J., 2010. Cohesive Properties and Asymptotics of the Dispersion Interaction in Graphite by the Random Phase Approximation. *Phys. Rev. Lett.* 105, 196401, <http://dx.doi.org/10.1103/PhysRevLett.105.196401>.
- Lee, C., Wei, X., Kysar, J.W., Hone, J., 2008. Measurement of the Elastic Properties and Intrinsic Strength of Monolayer Graphene. *Science* 321, 385–388, <http://dx.doi.org/10.1126/science.1157996>.
- Levy, N., Burke, S.A., Meaker, K.L., Panlasigui, M., Zettl, A., Guinea, F., Neto, A.H.C., Crommie, M.F., 2010. Strain-Induced Pseudo-Magnetic Fields Greater Than 300 T in Graphene Nanobubbles. *Science* 329, 544–547, <http://dx.doi.org/10.1126/science.1191700>.
- Li, X., Yang, W., Liu, B., 2007. Bending Induced Rippling and Twisting of Multiwalled Carbon Nanotubes. *Phys. Rev. Lett.* 98, 205502, <http://dx.doi.org/10.1103/PhysRevLett.98.205502>.
- Lindberg, H.E., 2003. Little Book of Dynamic Buckling. LCE Science/Software.
- Liu, J.Z., 2002. *Studies on Several Mechanical Problems of Carbon Nanotubes*. Tsinghua University, Beijing.
- Liu, J.Z., Zheng, Q., Jiang, Q., 2003. Effect of bending instabilities on the measurements of mechanical properties of multiwalled carbon nanotubes. *Phys. Rev. B* 67, 075414, <http://dx.doi.org/10.1103/PhysRevB.67.075414>.
- Liu, J.Z., Zheng, Q., Jiang, Q., 2001. Effect of a Rippling Mode on Resonances of Carbon Nanotubes. *Phys. Rev. Lett.* 86, 4843–4846, <http://dx.doi.org/10.1103/PhysRevLett.86.4843>.
- Liu, J.Z., Zheng, Q.-S., Wang, L.-F., Jiang, Q., 2005. Mechanical properties of single-walled carbon nanotube bundles as bulk materials. *J. Mech. Phys. Solids* 53, 123–142, <http://dx.doi.org/10.1016/j.jmps.2004.06.008>.
- Liu, Y., Xu, Z., Zheng, Q., 2011. Journal of the Mechanics and Physics of Solids. *J. Mech. Phys. Solids* 59, 1613–1622, <http://dx.doi.org/10.1016/j.jmps.2011.04.014>.
- Liu, Z., Liu, J.Z., Cheng, Y., Li, Z., Li, Z., Wang, L., Zheng, Q., 2012. Interlayer binding energy of graphite: a mesoscopic determination from deformation. *Phys. Rev. B* 85, 205418, <http://dx.doi.org/10.1103/PhysRevB.85.205418>.
- Liu, Z., Zheng, Q.-S., Liu, J.Z., 2010. Stripe/kink microstructures formed in mechanical peeling of highly orientated pyrolytic graphite. *Appl. Phys. Lett.* 96, 201909, <http://dx.doi.org/10.1063/1.3422484>.
- Malko, D., Neiss, C., Viñes, F., Görling, A., 2012. Competition for Graphene: Graphynes with Direction-Dependent Dirac Cones. *Phys. Rev. Lett.* 108, 086804, <http://dx.doi.org/10.1103/PhysRevLett.108.086804>.
- Mounet, N., Marzari, N., 2005. First-principles determination of the structural, vibrational and thermodynamic properties of diamond, graphite, and derivatives. *Phys. Rev. B* 71, <http://dx.doi.org/10.1103/PhysRevB.71.205214>, 205214–205214.
- Nair, R.R., Ren, W., Jalil, R., Riaz, I., Kravets, V.G., Britnell, L., Blake, P., Schedin, F., Mayorov, A.S., Yuan, S., Katsnelson, M.I., Cheng, H.M., Strupinski, W., Bulusheva, L.G., Okotrub, A.V., Grigorieva, I.V., Grigorenko, A.N., Novoselov, K.S., Geim, A.K., 2010. Fluorographene: A Two-Dimensional Counterpart of Teflon. *Small* 6, 2877–2884, <http://dx.doi.org/10.1002/sml.201001555>.
- Nicolosi, V., Chhowalla, M., Kanatzidis, M.G., Strano, M.S., Coleman, J.N., 2013. Liquid Exfoliation of Layered Materials. *Science* 340, 1226419, <http://dx.doi.org/10.1126/science.1226419>.
- Novoselov, K.S., Geim, A.K., Morozov, S.V., Jiang, D., Zhang, Y., Dubonos, S.V., Grigorieva, I.V., Firsov, A.A., 2004. Electric Field Effect in Atomically Thin Carbon Films. *Science* 306, 666–669, <http://dx.doi.org/10.1126/science.1102896>.
- Nye, J.F., 1985. *Physical Properties of Crystals*. Oxford University Press, New York.
- Plimpton, S., 1995. Fast parallel algorithms for short-range molecular dynamics. *J. Comput. Phys.* 117, 1–19, <http://dx.doi.org/10.1006/jcph.1995.1039>.
- Pocivavsek, L., Dellsy, R., Kern, A., Johnson, S., Lin, B., Lee, K.Y.C., Cerda, E., 2008. Stress and Fold Localization in Thin Elastic Membranes. *Science* 320, 912–916, <http://dx.doi.org/10.1126/science.1154069>.
- Poncharal, P., Wang, Z.L., Ugarte, D., de Heer, W.A., 1999. Electrostatic Deflections and Electromechanical Resonances of Carbon Nanotubes. *Science* 283, 1513–1516, <http://dx.doi.org/10.1126/science.283.5407.1513>.
- Price, N.J., Cosgrove, J.W., 1990. *Analysis of Geological Structures*. Cambridge University Press, United Kingdom.
- Qiu, L., Liu, J.Z., Chang, S.L.Y., Wu, Y., Li, D., 2012. Biomimetic superelastic graphene-based cellular monoliths. *Nat. Commun.* 3, 1241, <http://dx.doi.org/10.1038/ncomms2251>.
- Ren, M., Liu, Z., Zheng, Q.-S., Liu, J.Z., 2015. Mechanical buckling induced periodic kinking/stripe microstructures in mechanically peeled graphite flakes from HOPG. *Acta Mech. Sin.*, 1–6, <http://dx.doi.org/10.1007/s10409-015-0417-6>.
- Rogers, J.A., Someya, T., Huang, Y., 2010. Materials and Mechanics for Stretchable Electronics. *Science* 327, 1603–1607, <http://dx.doi.org/10.1126/science.1182383>.
- Schedin, F., Geim, A.K., Morozov, S.V., Hill, E.W., Blake, P., Katsnelson, M.I., Novoselov, K.S., 2007. Detection of individual gas molecules adsorbed on graphene. *Nat. Mater.* 6, 652–655, <http://dx.doi.org/10.1038/nmat1967>.
- Singh, S.K., Neek-Amal, M., Costamagna, S., Peeters, F.M., 2013. Thermomechanical properties of a single hexagonal boron nitride sheet. *Phys. Rev. B* 87, 184106–184107, <http://dx.doi.org/10.1103/PhysRevB.87.184106>.
- Song, L., Ci, L., Lu, H., Sorokin, P.B., Jin, C., Ni, J., Kvashnin, A.G., Kvashnin, D.G., Lou, J., Yakobson, B.I., Ajayan, P.M., 2010. Large scale growth and characterization of atomic hexagonal boron nitride layers. *Nano Lett.* 10, 3209–3215, <http://dx.doi.org/10.1021/nl1022139>.
- Sorella, S., Spanu, L., Galli, G., 2009. Nature and Strength of Interlayer Binding in Graphite. *Phys. Rev. Lett.* 103, 196401, <http://dx.doi.org/10.1103/PhysRevLett.103.196401>.
- Stafford, C.M., Harrison, C., Beers, K.L., Karim, A., Amis, E.J., VanLandingham, M.R., Kim, H.-C., Volksen, W., Miller, R.D., Simonyi, E.E., 2004. A buckling-based metrology for measuring the elastic moduli of polymeric thin films. *Nat. Mater.* 3, 545–550, <http://dx.doi.org/10.1038/nmat1175>.
- Stuart, S.J., Tutein, A.B., Harrison, J.A., 2000. A reactive potential for hydrocarbons with intermolecular interactions. *J. Chem. Phys.* 112, 6472.
- Tan, P.H., 2012a. The shear mode of multilayer graphene. *Nat. Mater.* 11, 294–300, <http://dx.doi.org/10.1038/nmat3245>.
- Tan, P.H., 2012b. The shear mode of multilayer graphene. *Nat. Mater.* 11, 294–300, <http://dx.doi.org/10.1038/nmat3245>.
- Tersoff, J., 1989. Modeling solid-state chemistry: Interatomic potentials for multicomponent systems. *Phys. Rev. B* 39, 5566–5568.
- Timoshenko, S.P., Gere, J.M., 2012. *Theory of Elastic Stability*. Courier Dover Publications, Mineola.
- Vogt, P., De Padova, P., Quaresima, C., Avila, J., Frantzeskakis, E., Asensio, M.C., Resta, A., Ealet, B., Le Lay, G., 2012. Silicene: compelling experimental evidence for graphenelike two-dimensional silicon. *Phys. Rev. Lett.* 108, 155501, <http://dx.doi.org/10.1103/PhysRevLett.108.155501>.
- Volkova, E.I., Jones, I.A., Brooks, R., Zhu, Y., Bichoutskaia, E., 2012. Sequential multiscale modelling of SiC/Al nanocomposites reinforced with WS₂ nanoparticles under static loading. *Phys. Rev. B* 86, 104111, <http://dx.doi.org/10.1103/PhysRevB.86.104111>.
- Wadee, M.A., Hunt, G.W., Peletier, M.A., 2004. Kink band instability in layered structures. *J. Mech. Phys. Solids* 52, 1071–1091, <http://dx.doi.org/10.1016/j.jmps.2003.09.026>.
- Wang, L., Zheng, Q., Liu, J.Z., Jiang, Q., 2005. Size dependence of the thin-shell model for carbon nanotubes. *Phys. Rev. Lett.* 95, 105501, <http://dx.doi.org/10.1103/PhysRevLett.95.105501>.
- Wang, L.-F., Zheng, Q.-S., 2007. Extreme anisotropy of graphite and single-walled carbon nanotube bundles. *Appl. Phys. Lett.* 90, 153113, <http://dx.doi.org/10.1063/1.2722057>.
- Wang, Q.H., Kalantar-Zadeh, K., Kis, A., Coleman, J.N., 2012. Electronics and optoelectronics of two-dimensional transition metal dichalcogenides. *Nature* 7, 699–712, <http://dx.doi.org/10.1038/nnano.2012.193>.
- Wang, Y., Yang, R., Shi, Z., Zhang, L., Shi, D., Wang, E., Zhang, G., 2011. Super-elastic graphene ripples for flexible strain sensors. *ACS Nano* 5, 3645–3650, <http://dx.doi.org/10.1021/nn103523t>.
- Wilson, J.A., Yoffe, A.D., 1969. The transition metal dichalcogenides discussion and interpretation of the observed optical, electrical and structural

- properties. *Adv. Phys.* 18, 193–335, <http://dx.doi.org/10.1080/00018736900101307>.
- Xu, Z., Xue, K., Xue, K., 2009. Engineering graphene by oxidation: a first-principles study. *Nanotechnology* 21, 045704, <http://dx.doi.org/10.1088/0957-4484/21/4/045704>.
- Yakobson, B.I., Brabec, C.J., Bernholc, J., 1996. Nanomechanics of carbon tubes: instabilities beyond linear response. *Phys. Rev. Lett.* 76, 2511–2514.
- Yu, M.F., 2004. Fundamental mechanical properties of carbon nanotubes: current understanding and the related experimental studies. *J. Eng. Mater. Technol.* 126, 271, <http://dx.doi.org/10.1115/1.1755245>.
- Zang, J., Ryu, S., Pugno, N., Wang, Q., Tu, Q., Buehler, M.J., Zhao, X., 2013. Multifunctionality and control of the crumpling and unfolding of large-area graphene. *Nat. Mater.* 12, 1–5, <http://dx.doi.org/10.1038/nmat3542>.
- Zartman, J.J., Shvartsman, S.Y., 2010. Unit operations of tissue development: epithelial folding. *Annu. Rev. Chem. Biomol. Eng.* 1, 231–246, <http://dx.doi.org/10.1146/annurev-chembioeng-073009-100919>.